Title

New Insights into Nonthermal Plasma-Assisted Poly(vinyl alcohol) Depolymerization Catalyzed by TiO2

Journal

The Journal of Physical Chemistry C, 129(10)

ISSN

1932-7447

Authors

Zhang, Heng

Oduntan, Aderinsola

Zhuo, Zengqing

et al.

Publication Date

2025-03-13

DOI

10.1021/acs.jpcc.4c07876

THE JOURNAL OF PHYSICAL CHEMISTRY C
A JOURNAL OF THE AMERICAN CHEMICAL SOCIETY

pubs.acs.org/JPCC

Article

New Insights into Nonthermal Plasma-Assisted Poly(vinyl alcohol) Depolymerization Catalyzed by TiO_2

Heng Zhang, Aderinsola Oduntan, Zengqing Zhuo, Steven S. C. Chuang,* Jinghua Guo,* and Jin Zhong Zhang*

Cite This: *J. Phys. Chem. C* 2025, 129, 4950−4963

Read Online

ACCESS | Metrics & More | Article Recommendations | Supporting Information

ABSTRACT: In this study, we investigated the solid residual poly(vinyl alcohol) (PVA) and TiO_2 after nonthermal air, CO_2, and N_2 plasma depolymerization in the absence and presence of TiO_2. Scanning electron microscopy studies showed the absence of highly viscous tar and carbonaceous residues on the surfaces of PVA and TiO_2. In the absence of TiO_2, PVA particles exhibited micron-sized holes on their surfaces, whereas in the presence of TiO_2, the surface roughness of PVA particles was observed at the submicron scale. These observations suggest that TiO_2 facilitates the even distribution of nonthermal plasma at a submicron scale, leading to a more uniform depolymerization of PVA surfaces. Raman, Fourier transform infrared spectroscopy, and X-ray absorption spectroscopy showed that (i) the surface of residual PVA contains mainly ketone functional groups and less C−H bonds than the pristine PVA and (ii) further confirmed the absence of highly viscous tar and carbonaceous residues on both used TiO_2 and residual PVA. The nuclear magnetic resonance and mass spectroscopy suggested that the PVA is growing back to poly polyvinyl acetate by the esterification reaction, and the ethers are produced by the acetal reaction between PVA and aldehyde. The transmission electron microscopy and X-ray diffraction analysis indicated no major crystal structural change of the TiO_2 catalyst after the plasma reactions. This study demonstrates that nonthermal plasma-assisted depolymerization is a viable alternative to thermal depolymerization, offering the unique advantage of converting polymer wastes into gaseous small organic molecules without generating recalcitrant viscous tar and carbonaceous residues on the surfaces of the polymer and TiO_2 catalysts.

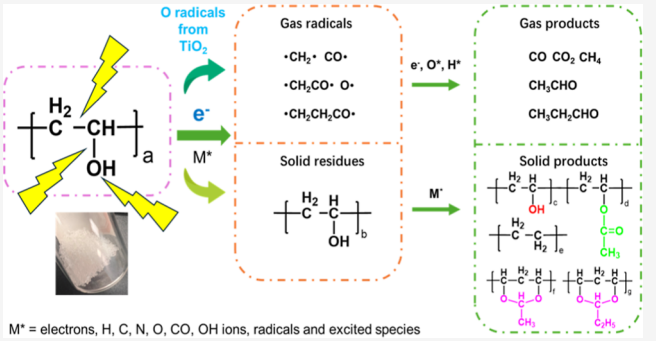

1. INTRODUCTION

Consumer polymers, also known as commodity polymers, have significantly benefited our society because of their low cost, lightweight nature, ease of processing, and durability. These characteristics have led to the widespread adoption of consumer polymers in numerous industries, including packaging, automotive, construction, electronics, and healthcare.[1−5] However, their durability poses substantial challenges for their disposal.[6−10] Polymer wastes enter our ecosystem, contaminating oceans and land, and infiltrating our food chain through microplastics.[11−13] Despite the seriousness of polymer waste pollution, efforts in upcycling and recycling polymer waste have been limited. For example, only about 5% of the 1 trillion plastic bags used annually in the US are recycled.[14,15]

A major obstacle to the recycling of polymer waste is downcycling, which produces materials of a lower value than the cost required for the recycling process. Thermal depolymerization methods, including pyrolysis and catalytic cracking, can be considered upcycling under specific conditions where high yields of high-value small organic molecules are generated. However, these methods require high thermal energy, i.e., high temperatures (over 300 °C), to break polymer bonds, and face challenges in the disposal of carbonaceous species, coking, and tar formation.[16,17] Depolymerization at lower temperatures could alleviate these issues. Many nonthermal plasma-assisted depolymerizations have shown a wide range of gas, liquid, and solid products, depending on the type of polymer, plasma, and operating conditions.[16−20] These studies are summarized in Table S1. However, most plasma-treated polymers show tar or coke products, or they do not report the related information. This hinders further practical applications in the industry as the carbonaceous species, coking, and tar can cover the catalyst and container surface, mix with products, and make the container hard to clean up and catalyst and valuable products

Received: November 21, 2024
Revised: January 29, 2025
Accepted: February 19, 2025
Published: February 28, 2025

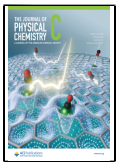

challenging to separate.[21,22] In addition, the conventional thermal cracking method, which consumes huge energy, produces heavy pollution and is against the green economy and environment nowadays.

We have recently conducted low-temperature depolymerization of poly(vinyl alcohol) (PVA) with nonthermal air and nitrogen plasma generated by dielectric barrier discharge (DBD) in the presence and absence of TiO_2.[10] PVA was used as a model polymer because of its variety of chemical bonds: C−C, C−H, C−O, and O−H; TiO_2 was used because of its partial and total oxidation activity as well as its stability.[23] The high energy electrons in the plasma can break down the chemical bonds and actively react with the gas reactants and generate excited species, such as, free radicals, excited atoms, ions, and molecules, followed by the initial chemical reaction in the depolymerization process.[24,25] The major gaseous products were found to be acetaldehyde, propionaldehyde, methane, CO_2, and CO. The presence of oxygen and TiO_2 can further enhance the yields of aldehyde products. A key issue remaining to be addressed is the residual polymers and catalysts. Are there byproducts such as carbonaceous species, coke, and tar present on the surface of polymers and catalysts? The presence of these species will significantly decrease the activity of nonthermal plasma in contacting the raw polymer waste for depolymerization; the presence of these species on the TiO_2 surface will impede its catalytic activity.

In this study, residual polymers with and without TiO_2 as a catalyst after nonthermal air, CO_2, and N_2 plasma-assisted depolymerization were characterized using an array of techniques, including scanning electron microscopy (SEM), transmission electron microscopy (TEM), X-ray diffraction (XRD), Raman, Fourier transform infrared (FTIR), X-ray absorption spectroscopy (XAS), nuclear magnetic resonance (NMR), and mass spectroscopy (MS). SEM images showed the absence of highly viscous tar and carbonaceous residues on the surface of PVA and TiO_2, and the presence of TiO_2 enables the surface roughness of PVA particles at the submicron scale, indicative of even distribution of nonthermal plasma and depolymerization reaction on the PVA surface. Raman, FTIR, and XAS spectroscopy showed evidence of decreased alcohol groups and generated ketone groups in residual PVA. The NMR and MS suggested the poly polyvinyl acetate (PVAc) and the cyclic cross-linking ether structures such as PVA−PVAc-PVA-acetal (O−CH_3CH_2−O) and PVA−PVAc-PVA-propional (O−$CH_3CH_2CH_2$−O). For the catalyst TiO_2, the TEM and XRD analyses indicated no major crystal structural change of the TiO_2 catalyst after the plasma reactions.

2. EXPERIMENTAL SECTION

2.1. Materials. PVA (M_W = 95,000 g/mol, Acros-Organics−average size 400 μm) and titanium(IV) oxide (Anatase, Sigma-Aldrich, <25 nm particle size) were used as received. CO_2 (99.999%) and N_2 (99.999%) gases were purchased from Praxair, Linde. The PVA−TiO_2 mixture in the 2:1 and 4:1 molar ratio was mixed and shaken well before being put into the nonthermal plasma reactor.

2.2. Raman Spectroscopy. Raman analysis was performed using a Thermo Fisher DRX3 Raman micro spectrometer. The laser excitation source was a diode laser (λex = 785 nm). Spectra were recorded under the following conditions: stainless-steel substrate, 50× objective, collect exposure time 30 s for five accumulations, laser power 30 mW (in focus), and aperture 50 μm slit.

2.3. FTIR Spectroscopy. The FTIR spectra for solid products were collected via the PerkinElmer FTIR spectrum two series spectrometer on a universal ATR sampling accessory (UATR). This solid FTIR uses a high refractive index diamond to apply pressure on the solid samples and guide the beam to the samples up to a few microns. To make the IR signal intensities consistent, the pressure applied to all of the solid samples is around 100.

2.4. XAS Spectroscopy. Soft X-ray absorption spectroscopy experiments were conducted for the C K-edge at beamlines 7.3.1 and 7.3.1 in the advanced light source (ALS) at Lawrence Berkeley National Laboratory. In this facility, the bending magnet beamline 7.3.1 provides a linearly polarized photon beam with an energy range from 250 to 1500 eV. The polymer samples were cut to 3 mm × 3 mm size and attached to the copper tape on a copper sample holder. A narrow copper tape was also attached to the surface of the samples to increase the conductivity of electrons from the sample's surface to the sample holder. All spectra for PVA were recorded using both total electron yield (TEY) and total fluorescence yield modes, while the C spectra were shown exclusively in the TEY mode due to a better signal-to-noise ratio. The energy positions of the C K-edge were calibrated using standard samples, HOPG.

2.5. SEM Measurement. We used different methods to prepare the samples for the SEM measurement. For PVA and PVA−TiO_2 mixture samples, they were sputtered with ∼20 nm of gold before the measurement and imaged in an FEI Quanta 3D Dualbeam SEM operating at 5 kV and 6.7 pA.

For TiO_2 powders, 1 mg of them was dispersed in 15 mL of methanol under ultrasound for 15 min before the measurement. All the suspension solutions were further dropped onto a hexagonal, 400 mesh copper grid coated with carbon film of standard 3−4 nm thickness (electron microscopy sciences, CF400H−Cu−UL) and allowed to dry in an ambient environment. The samples were imaged in an FEI Quanta 3D Dual Beam SEM operating at 5 kV and 6.7 pA later.

2.6. TEM Measurement. We used the same prepared TiO_2 powder samples from the SEM measurements for the TEM characterization. TEM and high-resolution TEM (HRTEM) were performed at the national center for electron microscopy (NCEM) at the Lawrence Berkeley National Laboratory Molecular Foundry on an FEI UT Tecnai microscope operated at 200 kV acceleration voltage. The images were analyzed with a Gatan Digital Microscope and ImageJ software.

2.7. XRD Measurement. The TiO_2 powders were rubbed and shaken to separate from the PVA mixture samples. XRD patterns were collected on a Bruker D8 Discover Diffractometer using Cu Ka radiation (40 kV and 40 mA) with degrees per step and time/step parameters of 0.02 deg/step and 0.4 s/step, respectively, at 2θ angle from 10 to 80°. X-ray diffraction patterns were plotted in Origin, and the XRD diffraction pattern of the PVA anatase phase was compared to JCPDS PDF no. 21-1272 extracted from Jade software.

2.8. NMR Measurement. The PVA mixture samples were washed to remove the TiO_2 powder on the surface. 10 mg of separated PVA crystals was dissolved in 0.5 mL of DMSO-d_6 with an elevated temperature at 90 °C, and the solution was filtered with cotton for the final characterization. The NMR data were collected on a Bruker AVANCE III HD 500 MHz NMR instrument equipped with a BBFO broadband probe. Both the 1D proton and carbon experiments were collected by

https://doi.org/10.1021/acs.jpcc.4c07876
J. Phys. Chem. C 2025, 129, 4950−4963

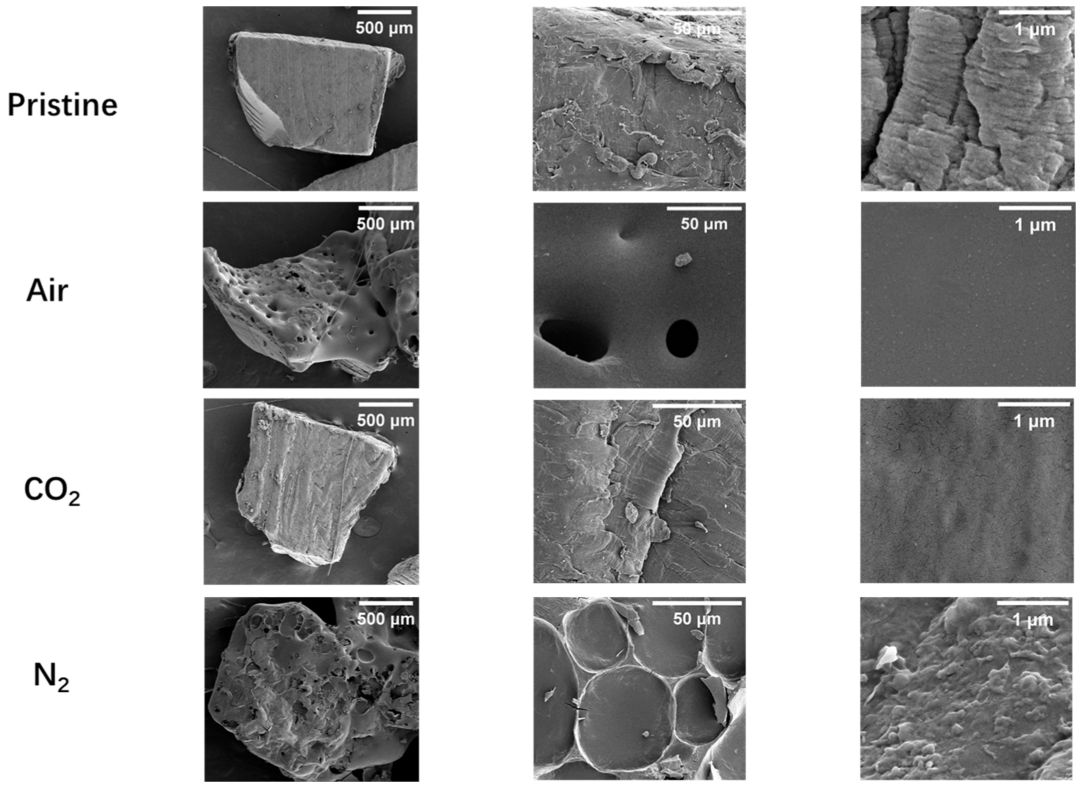

Figure 1. SEM images of the pure PVA crystals without catalyst addition before and after air, CO_2, and N_2 nonthermal plasma at 25 °C.

using pulse programs from the Bruker pulse program library. The 1D proton experiment was collected using a spectral width of 10000.0 Hz with acquisition time of 3.2768 s, 1 s recycle delay, and 16 scans at 300 K. The 1D Carbon experiment was collected using a spectral width of 29761.9 Hz with acquisition time of 1.1010 s, 2 s recycle delay, and 1024 scans at 300 K. The data were processed using Mestrenova.

2.9. Matrix-Assisted Laser Desorption/Ionization Mass Spectroscopy (MALDI-MS) Measurement. MALDI-MS analyses were conducted with a Bruker Microflex MALDI-LT (linear time-of-flight) instrument. The matrix and sample were mixed together and deposited on the stainless steel, and the concentrations were as follows: matrix: saturated DHB (2,5-dihydroxybenzoic acid) solution dissolved in 78:22 Milli-Q H_2O: ACN + 0.1% TFA with a concentration around 30 mg/mL; PVA sample: dissolved in H_2O at 10 mg/mL concentration. The analyses were performed in the linear mode. The measurement was calibrated with a standard reference, phosphorus red, used in the protein. Detection ranges from 200 to 1100 and 2000 to 19,000 Da. The data were originally processed and saved in the XML format in FlexControl software and converted to the mzXML format in the MSConvertGUI application program downloaded from the ProteoWizard Website. The mzXML files were opened, processed, and exported as CSV files in the MALDIquant package running on the R platform comprising all steps from importing of raw data, preprocessing (e.g., baseline removal), peak detection, and nonlinear peak alignment to calibration of mass spectrograph. Some codes to run the functions in R with the MALDIquant package were from ChatGPT with modifications. The CSV files were opened in Excel and replotted in Origin software.

3. RESULTS AND DISCUSSION

3.1. Nonthermal Plasma Effect on the PVA−TiO_2 Mixture. The PVA and PVA−TiO_2 mixtures were first characterized using SEM to determine the plasma effect on the surface area with and without catalyst TiO_2. As is well-known, surface structure is vital in catalysis reactions, and unfavorable morphology will decrease or disable the catalyst function, leading to a low efficiency in the polymer depolymerization reactions. The reason is that the catalyst surface acts as an essential diffusion pathway for all the plasma species, and the active sites on the surface area are critical to promote the reaction time and efficiency in the catalysis reaction.[17,19] According to the Mars-van Krevelen mechanism, the organic molecules like PVA adsorbed on metal oxides (such as TiO_2) surface are oxidized by oxygen radicals (atoms) emerging from the crystal lattice of TiO_2 and then the reduced metal oxides (such as TiO_{2-x}) are oxidized back to TiO_2 by uptake of gaseous oxygen, which is crucial for the oxidative depolymerization of PVA.[26] Also, by enhancing the dispersion of reactant aided by the catalyst, further with the nonthermal process, we expect the homogeneous reaction on the polymer surface; thus, coking and tar formation will be alleviated.

Figure 1 shows SEM images of the pure PVA crystals before and after different plasma reactions. The images show that the PVA sizes are around 0.5−1 mm, and the crystals are in cuboid shape. Except for the pristine sample, erosion effects are present on the surface of all other samples, including the holes for the air-plasma-treated sample, the ridges for the CO_2 plasma-treated sample, and pits for the N_2 plasma-treated sample. At 1 μm scale bar, the pristine sample shows the original defects on the surface; however, the PVA surface treated under N_2 plasma presents some viscous substance-like structures, probably related to the coalescence of scissored

https://doi.org/10.1021/acs.jpcc.4c07876
J. Phys. Chem. C 2025, 129, 4950−4963

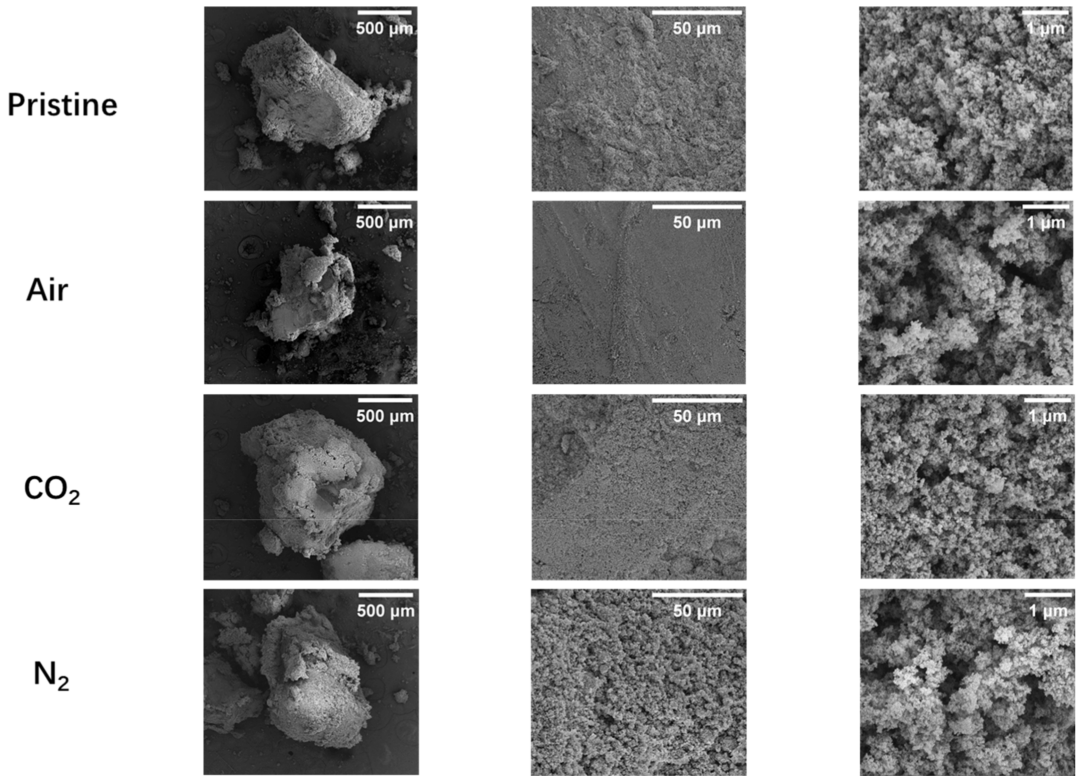

Figure 2. SEM images of PVA−TiO_2 mixture (2:1 molar ratio) samples before and after air, CO_2, and N_2 nonthermal plasma reactions at 25 °C.

chain structures.[27] These images show that the plasma species attack the surface and even inside of PVA, indicating the bond breaking in the microscale. More images of the reacted spots on the surface are shown in Figure S2.

Figure 2 shows the SEM images of the PVA−TiO_2 mixture samples before and after different plasma reactions. The images at low magnification (500 μm) show that the PVA surface is covered by powder clusters of different thicknesses. After enlarging the images with a 50 μm scale bar, undestroyed plain surfaces were observed without holes, ridges, or pits compared to the treated pure PVA crystals in Figures 1 and S2. This result is significant and demonstrates an even reaction that happened on the surface with the aid of catalyst TiO_2 powders. By looking at the morphology in high resolution (1 μm), the materials hold similar spherical morphology, confirming that they are the TiO_2 particles other than decomposed small pieces of PVA polymers on the surface. Figure S3 shows that the PVA−TiO_2 4:1 mixture samples exhibit a similar effect. By comparing Figures 1, 2 and S3, TiO_2 helps in achieving a more homogeneous reaction on the polymer surface, which showed that deep craters with the size of 10−50 μm were produced in the absence of TiO_2 in nonthermal air plasma. It is interesting to observe shallow craters with the size of 30−50 μm in the absence of TiO_2 in nonthermal N_2 plasma. TiO_2 enhanced the rate of reaction and produced more uniform PVA surfaces. Notably, another key observation from the SEM results is the absence of coke or tar formation in the TiO_2-assisted nonthermal polymer depolymerization.

3.2. Nonthermal Plasma Effect on Catalyst TiO_2.

Figure 3 shows the morphology of TiO_2 powders separated from the PVA−TiO_2 mixture (2:1 molar ratio) before and after the air, CO_2, and N_2 plasma reactions. When focusing on a low resolution (1 μm scale bar), we can see that the clusters of the powders are in different shapes. After zooming in to a higher resolution (100 nm scale bar), individual TiO_2 powder particles can be observed, and their size is around 10−20 nm. By comparing the powders in different reaction conditions, the pristine ones have more homogeneous spherical shapes, while the powders treated in other conditions

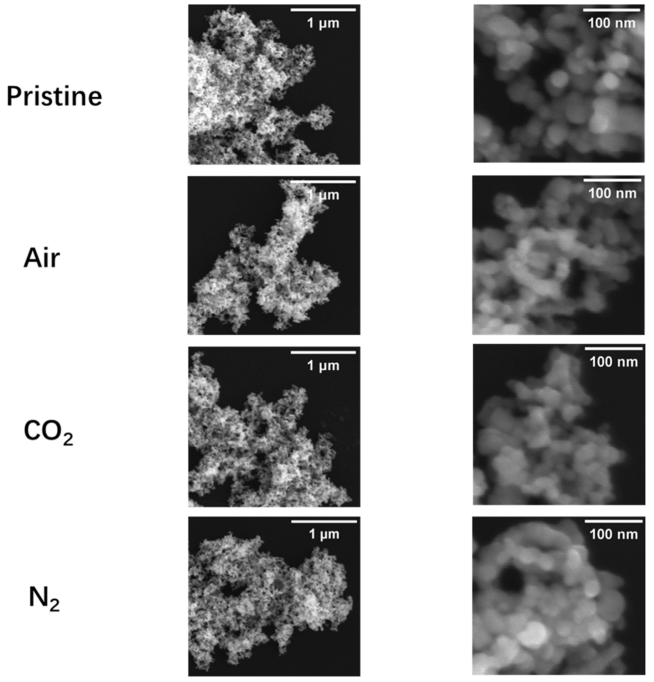

Figure 3. SEM images at low magnifications (1 μm) and high magnifications (100 nm) of the TiO_2 powders separated from PVA−TiO_2 mixture (2:1 molar ratio) before and after air, CO_2, and N_2 nonthermal plasma reaction at 25 °C.

https://doi.org/10.1021/acs.jpcc.4c07876
J. Phys. Chem. C 2025, 129, 4950−4963

(air, CO_2, and N_2 plasma) show smaller sizes and links between the powders. However, there are no major morphology or shape changes observed for the individual particles after the reactions. A similar morphology of the TiO_2 powers was also observed in the PVA−TiO_2 4:1 ratio in Figure S4. Through more refined morphology and structural study via TEM (see Figures S5 and S6), the results of no significant morphology or shape changes are consistent with our SEM findings.

To further evaluate the catalyst properties after the plasma reactions, Raman spectra were acquired to determine the chemical structure changes. Figure 4 presents the Raman peaks

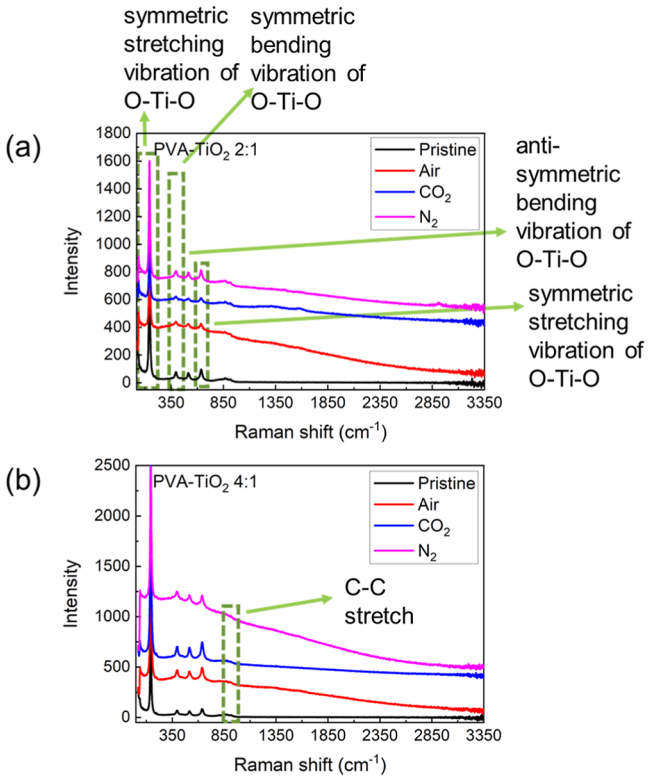

Figure 4. Raman spectra of TiO_2 powders separated from PVA−TiO_2 mixture in the (a) 2:1 molar ratio and (b) 4:1 molar ratio before and after air, CO_2, and N_2 nonthermal plasma reaction at 25 °C. The green boxes show the same peak position among different conditions.

of TiO_2 in PVA−TiO_2 2:1 and 4:1 ratios before and after the gas plasma reactions. The four signature peaks at 142, 398, 513, and 640 cm^{-1} are associated with symmetric stretching vibration, symmetric bending vibration, antisymmetric bending vibration, and symmetric stretching vibration of Ti−O−Ti bond and agree well with the anatase phase.[28−31] The sharp peaks for the symmetric stretching vibration of the Ti−O−Ti bond stand out and retain high intensity after the reaction studies. The increased intensity of the 142 cm^{-1} peak after nonthermal N_2 reaction indicates changes in the surface structure of the TiO_2 catalyst, likely due to surface cleaning, nitrogen incorporation, defect passivation, or enhanced crystallinity.[32−35] Meanwhile, the intensity ratio among the three peaks in the 350−850 cm^{-1} region remains the same for all of the samples, indicating that the Ti−O−Ti bond remains stable and intact. Also, the increased background for the samples treated with plasma was noticed and it could be due to the degradation effect of PVA (−CH_2−CHOH−), and some solid residues are left on the surface of the catalyst indicated by the C−C stretch vibration at 865 cm^{-1}, in turn, implying that the catalyst surface was involved in the plasma-assisted polymer degradation.[36,37] This chemical structure study demonstrates the high stability of the catalyst TiO_2 used in the plasma reaction, without the deactivation caused by the accumulation of carbonaceous residues,[38] providing an excellent example of intermediates for nonthermal polymer depolymerization.

Figure 5 shows the XRD patterns of the TiO_2 powders before and after the plasma reactions. All XRD patterns

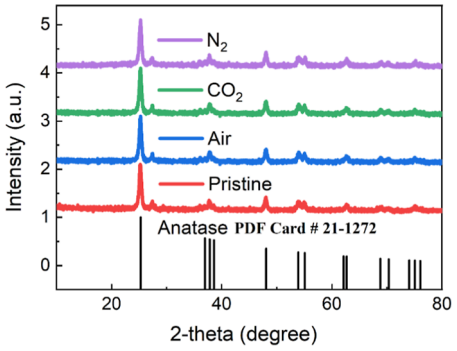

Figure 5. XRD pattern of TiO_2 powders at the pristine state and after air, CO_2, and N_2 plasma reactions. The TiO_2 anatase phase PDF card was put at the bottom of the figure for ref 42.

indicate a well-defined crystal structure of TiO_2 before and after the reactions. The diffraction peaks remain the same under different conditions, and peaks at 25.2, 37.8, 48.0, 54.0, 55.1, 62.7, 69.0, 70.3, and 75.1° assigned to (101), (004), (200), (105), (211), (204), (116), (220), and (215) diffraction planes match well with the anatase phase of TiO_2.[39−41] We can conclude that the crystal structure of the catalyst TiO_2 stays intact, and there are no O^{2-} holes induced local structure distortions under the plasma reactions.

3.3. Nonthermal Plasma Effect on PVA Solid Products. Figure 6 shows the Raman peaks of PVA, PVA separated from PVA−TiO_2 mixture in 2:1 and 4:1 molar ratios under air, CO_2, and N_2 nonthermal plasma reactions. In Figure 6a for the pristine PVA samples, after the gas plasma reactions, the peak at 2910 cm^{-1} assigned to the CH_2 stretch increases the intensity, suggesting the production of the CH_2 bond and the breaking of the C−OH bond in the (−CH_2−CHOH−) backbone at the same time.[43] Under the air and N_2 plasma conditions, a significantly increased background was observed, showing a high fluorescence intensity, which is due to the generated short fragments of depolymerized materials on the surface.[36,37] These results confirm that the depolymerization reaction occurred on the surface. In the N_2 plasma-treated samples, the intensity of peaks attributed to the C−OH vibrations decreases dramatically while the CH_2 bond intensity increases largely compared to the pristine samples, demonstrating the scission of the C−OH bond and hydrogenated to CH_2 in the structure, which was discussed in the gaseous products.[10] In conclusion, these Raman spectra indicate the cleavage of the C−OH bond in the repeating units of the PVA and of all the reaction conditions, N_2 plasma demonstrates the highest efficiency in breaking the C−OH group and generation of a further related function group, in line with the result of

https://doi.org/10.1021/acs.jpcc.4c07876
J. Phys. Chem. C 2025, 129, 4950−4963

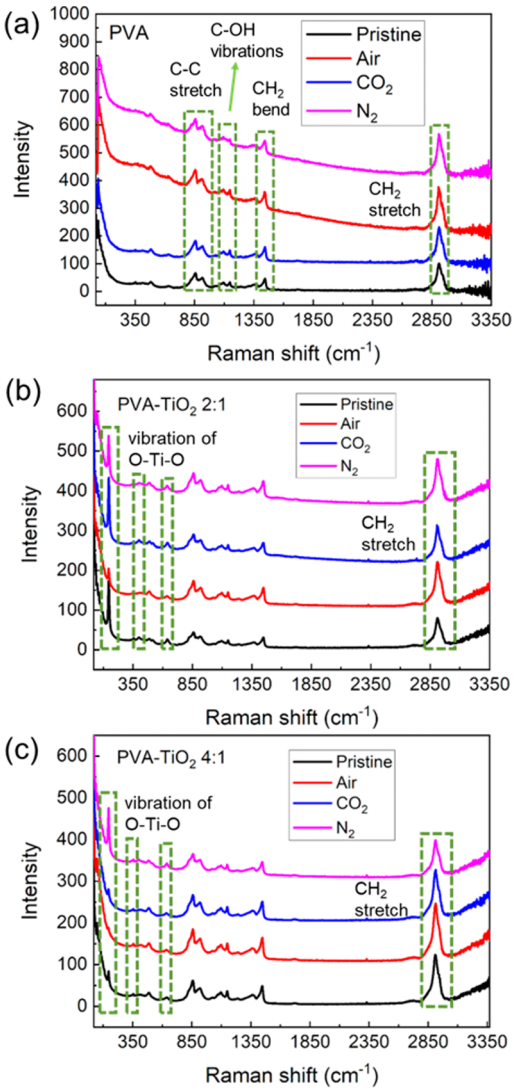

Figure 6. Raman spectra of PVA samples (a) without TiO_2 addition, (b) separated from PVA−TiO_2 2:1 molar ratio, and (c) separated from PVA−TiO_2 4:1 molar ratio before and after air, CO_2, and N_2 nonthermal plasma at 25 °C. The green boxes show the same peak position among different conditions.

higher selectivity to the aldehydes in N_2 plasma in the gaseous products.[10]

In Figure 6b,c, TiO_2 was added as a catalyst to promote the depolymerization efficiency. The PVA−TiO_2 samples were washed to separate PVA from the mixture before being characterized, although a small amount of the TiO_2 can still be found on the surface, as indicated by the vibration of Ti−O−Ti bond peaks. Since we are focusing on the PVA depolymerization after the reaction, the TiO_2 signals are the catalyst residual on the surface and will not be discussed here. For the samples with a PVA−TiO_2 2:1 ratio (Figure 6b), the intensity of peaks assigned to the C−C stretch, C−OH vibrations, CH_2 bend, and the CH_2 stretch increases by the same degree, implying the similar degradation effect on the solid samples. For the samples separated from a PVA−TiO_2 4:1 ratio (Figure 6c), the intensity of different peaks shows a trend similar to those with a PVA−TiO_2 2:1 ratio. All the spectra from both PVA−TiO_2 2:1 and 4:1 ratios do not show the fluorescence background, which could be due to the washing on the PVA surface. Nonetheless, in the gaseous products study, the TiO_2 catalysts enhanced the total oxidation of PVA to CO_2 evidenced by that decreasing the amount of TiO_2 (PVA−TiO_2 4:1 molar ratio) led to the return of aldehyde products and CO.[10] The aid of degradation or a selectivity effect was not observed in the solid products.

Figure 7 shows the FTIR spectra for PVA samples with and without TiO_2 under different plasma conditions to fully investigate the chemical structure. For the PVA samples in Figure 7a, we assigned the peaks at 3271, 2908, 1711, 1417, 1089, and 844 cm^{-1} to O−H stretching, CH stretching, C═O stretching, CH_2 bending, C−O stretching in the acetyl group, and C−C stretching vibrations, in conformity with earlier studies.[27,44−46] The O−H stretching vibration decreases after the plasma reaction, indicating that the cleavage of the O−H bond and the left H will be an active species for PVA decomposition reactions. Also, the decrease in the CH stretching intensity suggests that the CH−OH bone breaks down with the reaction. In the meantime, the increase of the C═O stretching vibration implies that more carbonyl groups have formed due to the reaction of the OH group. The original C═O stretching is attributed to the residual acetate group after the preparation of PVA from hydrolysis of polyvinyl acetate or oxidation during synthesis and processing.[44,45] The C−C bond intensity decreases after the plasma reactions, indicative of the PVA backbone cleavage. These results inform the fracture of the main structure and O−H bond with the formation of the C═O bond during which the N_2 plasma reaction exhibits the highest efficiency.

For the PVA samples treated with TiO_2 catalyst (PVA−TiO_2 2:1 and 4:1 ratio), we assigned the peaks 3272, 2909, 1714, 1417, 1089, and 844 cm^{-1} to O−H stretching, CH stretching, C═O stretching, CH_2 bending, C−O stretching in the acetyl group, and C−C stretching vibrations. The intensity of the O−H bond diminishes more with the aid of the catalyst TiO_2. A similar phenomenon that the decrease in the O−H bond and CH bond and the increase in the C═O bond is observed in the catalyst-treated samples. The C−C bond intensity in the PVA−TiO_2 4:1 ratio also decreases in the TiO_2-treated samples, implying the fracture of the PVA chains. With a higher amount (PVA−TiO_2 2:1) of the catalyst, CO_2 plasma enables an increased generation of the C═O bond. These results suggest the scission of the backbone and O−H bonds under plasma reactions, and the catalyst facilitates with CO_2 plasma reaction for carbonyl group generation but N_2 plasma helps with the OH bond cleavage. The specific molecules still need further study with techniques such as NMR and will be used later to show the structural change and possible detailed compound.

Figure 8 shows the C K-edge XAS spectra to determine the electronic state of the C element in PVA before and after the nonthermal plasma reactions. Across all conditions, the C K-edge XAS spectra exhibit a distinct splitting around 287 eV, with the peak at 287.3 eV assigned to σ^* (C−O−H) and the peak at 288.2 eV associated with the σ^* (C═O) bond.[47] Figure 8a displays C K-edge XAS collected on pure PVA samples, where the feature at 285 eV is assigned to the C 1s to C π^* transition in the C−C bond. Treatments under different conditions produce minimal changes in the backbone C−C structure. However, in the photon energy region near 287 eV, the intensity of the C*−O−H and C*═O bond peaks shows dramatic changes before and after treatment. The dominant contribution observed at 288.2 eV (Figure 8a) corresponds to

https://doi.org/10.1021/acs.jpcc.4c07876
J. Phys. Chem. C 2025, 129, 4950−4963

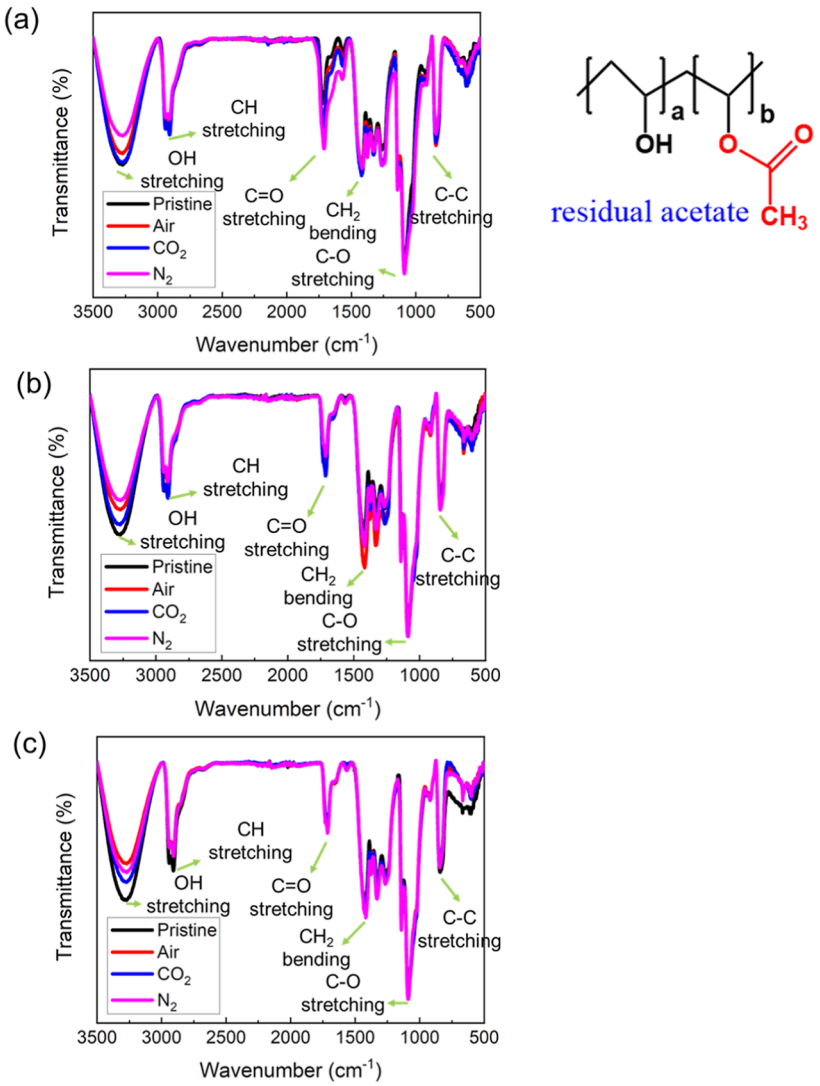

Figure 7. FTIR spectra of PVA samples (a) without TiO_2 addition, (b) separated from PVA−TiO_2 2:1 molar ratio, (c) separated from PVA−TiO_2 4:1 molar ratio before and after air, CO_2, and N_2 nonthermal plasma at 25 °C. The side images illustrate the hydrolyzation of PVA. The vinyl alcohol polymer and acetate are produced in a ratio of a and b in mol %, and b is significantly smaller than m due to the low concentration of residual acetate.

the C═O group, showing an increasing C*═O bond absorption signal in the sequence of air, CO_2, and N_2 plasma reactions, indicative of the reaction degree of the breaking of the C−OH bond and forming of the C═O bond and N_2 plasma reaction showing the highest efficiency.

Similar phenomena for C element-specific XAS spectra were observed in the PVA samples separated from the PVA-TiO_2 mixtures, where the C*═O bond absorption signal increased while the C*−OH bond absorption signal decreased, indicating the scission of the CO−H bond from the polymer main structure. In the PVA samples separated from PVA−TiO_2 2:1 ratio, air plasma is most effective in breaking the C−OH bond. In contrast, in PVA samples separated from the PVA−TiO_2 4:1 ratio, CO_2 exhibits the best conditions for this bond scission. Overall, the XAS data are consistent with the FTIR and Raman results, supporting the conclusion of C−OH to C═O conversion.

The comparative analysis of Raman, FTIR, and XAS spectroscopy reveals consistent findings regarding the effectiveness of PVA depolymerization in nonthermal plasma. N_2 plasma is particularly efficient in cleaving the C−OH bond and eliminating OH group from PVA in terms of solid products while when catalyst TiO_2 is present, air and CO_2 plasma is more active for CH_2 formation (alkylation) in Raman and FTIR and C═O generation (oxidization) by XAS spectra, probably due to the synergic effect of the O radicals arising from TiO_2 and air or CO_2 plasma. The catalytic role of TiO_2 in enhancing the depolymerization efficiency is evidenced clearly in FTIR and XAS results based on the decrease degree of the OH group compared to the pristine PVA. These complementary spectroscopic analyses provide a comprehensive understanding of depolymerization of PVA by nonthermal plasma.

Figure 9 shows the ^1H and ^{13}C NMR spectra of PVA samples in pristine, treated in N_2 plasma, and treated in N_2 plasma and TiO_2 catalyst for detailed structure determination. The assignments of the solvent, deuterated DMSO-d_6, and PVA signature chemical group are based on the previous reports.[45,48] In ^1H NMR spectra, the peaks for all of the signature chemical groups in PVA either decreased in TiO_2-assisted samples or changed shapes after the N_2 plasma reaction, showing the modification of the backbone to break

https://doi.org/10.1021/acs.jpcc.4c07876
J. Phys. Chem. C 2025, 129, 4950−4963

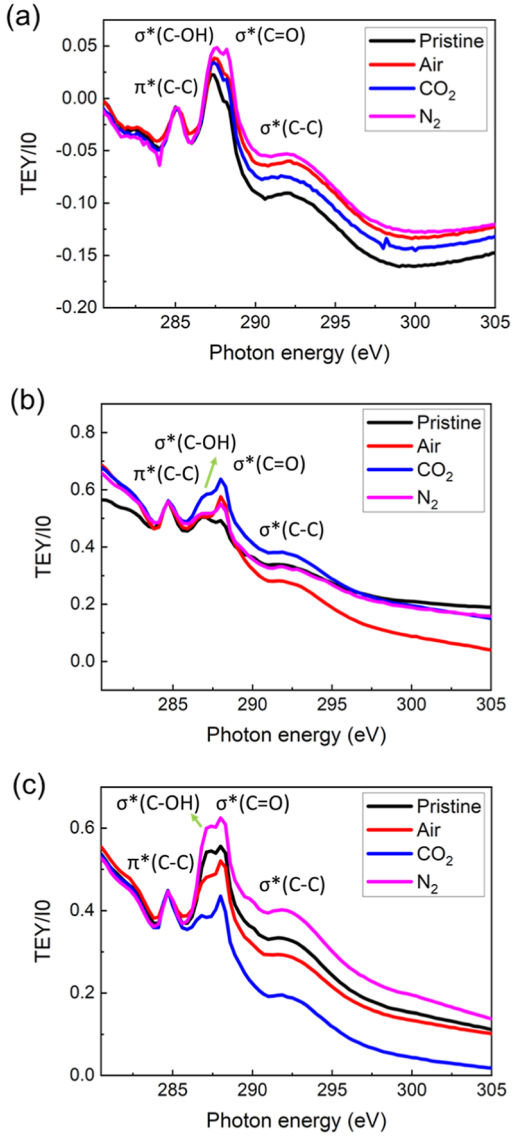

Figure 8. XAS spectra on C element of PVA samples (a) without TiO_2 addition, (b) separated from PVA- TiO_2 2:1 molar ratio, and (c) separated from PVA- TiO_2 4:1 molar ratio before and after air, CO_2, and N_2 nonthermal plasma at 25 °C.

down and generate new compounds. In the ^{13}C NMR spectra, the peak positions and intensities do not show significant changes after the N_2 plasma and catalyst (PVA−TiO_2 2:1) treatment, but there are decreased intensities for all the existing peaks and emerging new peaks in the PVA N_2 plasma condition. The TMS signal is from DMSO-d_6, and the variance from different spectra is from the two bottle sources with different concentrations of TMS. The ^1H NMR peaks at 1.4 and 3.6 ppm (middle spectra) are tentatively assigned to CH_2 and CH−O from PVAc (polyvinyl acetate). The ^{13}C NMR peaks at 19, 66, and 172 ppm in PVA treated in N_2 plasma match well with the reported data, showing the PVAc structure in the solid compounds.[49,50] The peak at 42.4 ppm is tentatively assigned to CH_2 from PVAc. The peak at 78.5 ppm is assigned to CH−O, the ether structure.[51,52] This result indicates that the plasma reaction provides an oxidation environment and oxidizes the PVA back to PVAc compared to the hydrolysis of PVAc during preparation in the factory. In the acid environment created by alcohol oxidation products, ethers are suggested to be produced. This result demonstrated that the sole N_2 plasma boosts the abundant reactions and creates the most products in the solid. The production of PVAc and ether is supported by our FTIR data with increased C═O bond and C−O bond intensity but without peak position changes.

Figure 10 shows the mass spectra of PVA in pristine, treated in N_2 plasma, and treated in N_2 plasma and TiO_2 catalyst to learn about the molecular weight of the decomposed products. All the PVA samples show the fragmented PVA in the low mass region, e.g., 200, 332, and 372 m/z, which is interpreted as 4, 7, and 8PVA units. Similarly, PVA reacted in N_2 plasma shows the most solid products and two new peaks at 618 and 860, respectively. These two peaks are assigned to PVA−PVAc and PVA−PVAc-PVA-acetal (O−CH_3CH_2−O) or PVA−PVAc-PVA-propional (O−$CH_3CH_2CH_2$−O), as shown in insets in MS of PVA reacted in N_2 plasma, although PVAc, PVA-acetal, or PVA-propional are in a small amount suggested from the mass spectrum. 887 m/z can be explained as the PVA−PVAc with 19 PVA units and 1 polyvinyl acetate unit and it is longer than the structure with a molecular weight of 618 Da, indicating that the catalyst TiO_2 can promote the PVAc production (618 Da) but with a larger molecular weight. This result aligns with the NMR results to support the production of PVAc and ether structures.

3.4. Depolymerization Mechanisms. The experimental results are summarized and discussed below to provide more insight into our study. Raman spectra exhibited that some C−OH groups are hydrogenated to CH_2 group solid products, implying the cracking of C−OH bond in the backbone. FTIR measurements confirmed the cleavage of the long chain to the short chain through the C−C bond breakage. The diminishing of the OH bond signal suggests its cleavage and the generation of free H species. Moreover, the decline of the C−OH group and the ascent of the C═O group in the spectra indicate the transformation of the alcohol group to the ketone group. When taking the charged species and radicals into account, the produced C, N, and O plasma species play an important role in oxidatively dehydrogenating the C−OH group. All the measurements, including Raman, FTIR, XAS, NMR, and MS, confirmed the formation of the carbonyl group and the viability and efficiency of nonthermal plasma to depolymerize the PVA. Extracted from all the information with the gaseous products study included, we conclude that the major reaction in the nonthermal plasma-assisted PVA depolymerization is the evolution of alcohol group to the ketone group and the following esterification and acetal reactions in the plasma environment. The gas plasma, including air, CO_2, and N_2 produces active species, such as radicals, ions, and electrons, attack the bonds and break down the main structure into shortened solid fragments and valuable small gas molecules.

In a former PVA solution study treated with gamma irradiation, a similar result that OH to C═O transition was extracted from FTIR and the breaking of C−H and C−OH bonds; therefore, the formation of more carbonyl double bonds (C═O) and the chain structure breaking was concluded. The water solution under γ radiation will generate electrons, ions, radicals, and molecules, such as e^-, H^+, H_3O^-, $H^\bullet$, $OH^\bullet$, H_2, and H_2O_2, similar to our gas plasma system.[44] This result supports our observation of the conversion of the alcohol group to the ketone group by the scission of the O−H and C−OH bonds and the formation of a C═O bond in the PVA main structure.

https://doi.org/10.1021/acs.jpcc.4c07876
J. Phys. Chem. C 2025, 129, 4950−4963

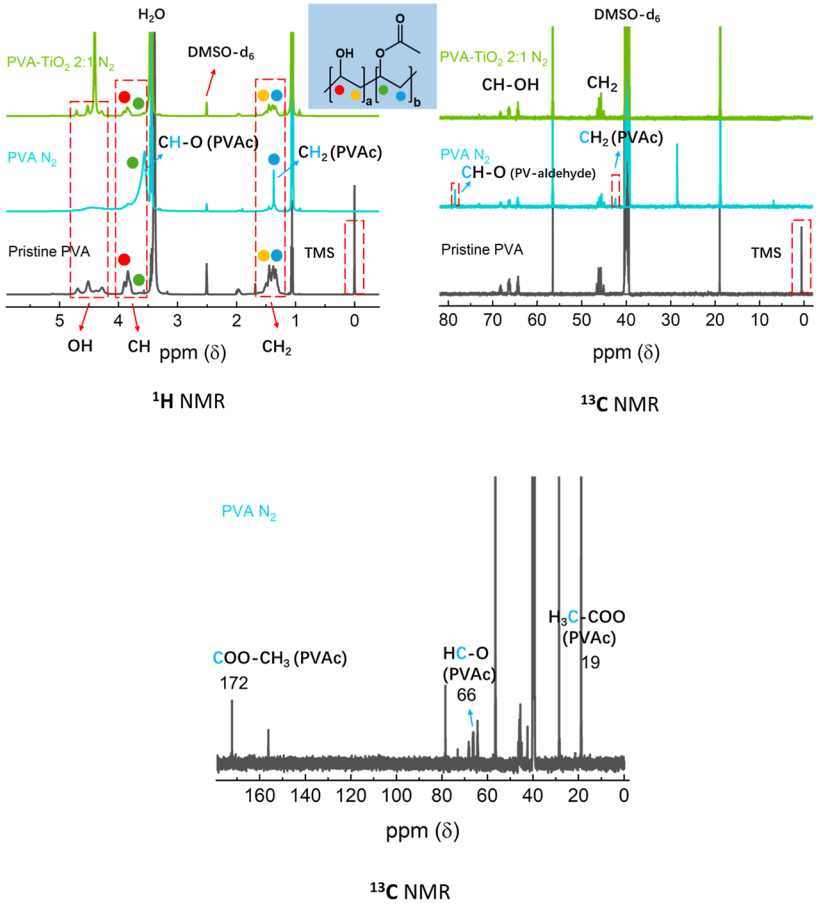

Figure 9. ^{1}H and ^{13}C NMR spectra of pristine PVA samples, PVA samples reacted under N_2 plasma, PVA samples separated from the PVA−TiO_2 mixture (2:1 molar ratio) reacted under N_2 plasma, and PVA samples reacted under N_2 plasma at large range (0−180 ppm).

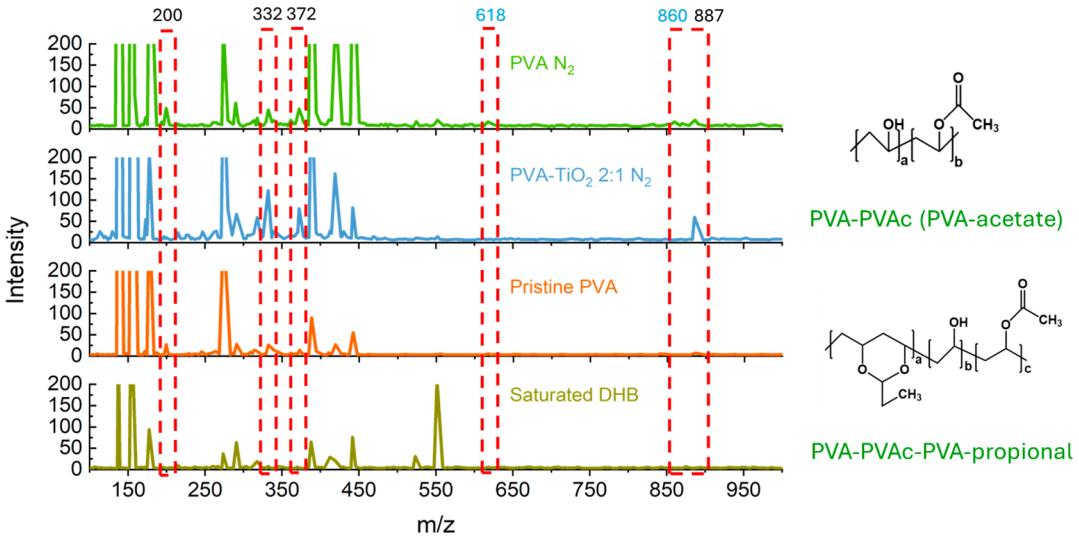

Figure 10. MALDI-mass spectra of matrix DHB (2,5-dihydroxybenzoic acid), pristine PVA samples, PVA samples reacted under N_2 plasma, and PVA samples separated from the PVA−TiO_2 mixture (2:1 molar ratio) reacted under N_2 plasma. Insets in MS of PVA reacted under N_2 plasma show PVA−PVAc and PVA−PVAc-PVA-propional structure.

Some researchers emphasized the electron impact effect to improve the polymer reforming in the nonthermal plasma reactions. Williams's group utilized the nonthermal plasma method to improve the biofuel quality during the treatment.[25,53] The improvement is attributed to high-energy electrons, excited radicals, ions, and intermediates that increase the interaction between the polystyrene and biomass pyrolysis volatiles. The chemical bonds in polymer and the gaseous products can be easily broken down by high-energy electrons or other excited species because these bonds have lower mean energies; for example, the C−H bond with a binding energy of 4.3 eV and the C−C bond of 3.4 eV in high-density

https://doi.org/10.1021/acs.jpcc.4c07876
J. Phys. Chem. C 2025, 129, 4950−4963

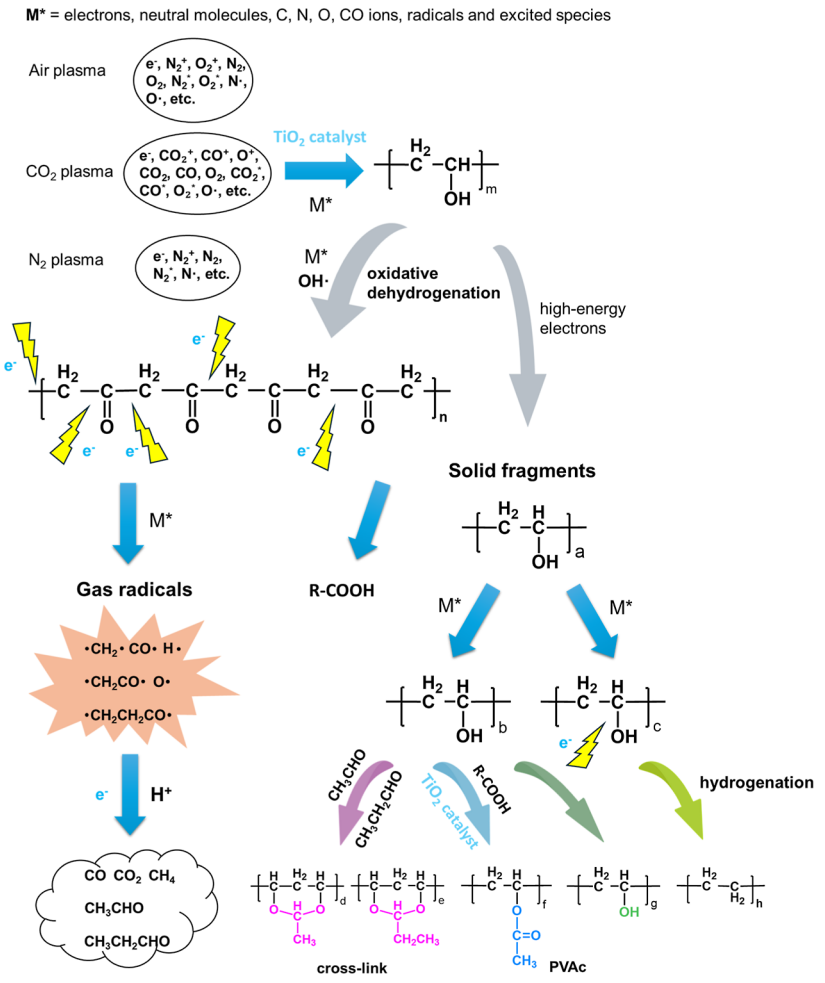

Figure 11. Proposed reaction pathways in the air, CO_2, and N_2 nonthermal plasma-assisted PVA degradation process.

polyethylene (HDPE) compared to the excited electrons (with high energy in the range of 0−10 eV) and N_2* (with an energy of 6.2 eV).[17,54] The covalent bond dissociation energies in the polyvinyl polymers are between 300 and 500 kJ mol^{-1} which corresponds to 3−5 eV in electronvolt unit, specifically C−C, 3.59 eV; C−O 3.71 eV; C−H 4.25 eV; and H−O 4.75 eV.[55] Furthermore, according to Meng et al., the high-energy electrons produced in the nonthermal plasma process facilitate the tar removal in the final products, which is also shown in this study.[56]

From the previous plasma studies, different gases will have different reactions under high voltages, for example, air plasma: $O_2 + e \rightarrow 2O + e$, $N_2 + e \rightarrow 2N + e$; CO_2 plasma: $CO_2 + e \rightarrow CO + O + e$, $CO + e \rightarrow C + O + e$; and N_2 plasma: $N_2 + e \rightarrow 2N + e$.[57−60] The electrons and C, N, O, and CO radicals are reactive atomic species and will dissociate the OH bond and have the H radicals as the reactive species.[61] Under air, CO_2, and N_2 conditions, the dominant reactive species are different, and bond scission mechanisms vary slightly. The different reaction mechanisms are summarized below.

Air plasma generates a mix of reactive oxygen species (ROS) such as atomic oxygen (O), ozone (O_3), hydroxyl radicals ($OH^•$), and superoxide (O_2^-).[62−64] These species are highly effective in initiating partial oxidation of polymers that incorporate oxygen atoms into the polymer structure, leading to functional groups such as ketones, aldehydes, or carboxylic acids. In contrast, total oxidation to CO_2 is less favored due to the competition between reaction pathways and the limited availability of ROS under typical nonthermal plasma conditions. Air plasma facilitates a broad range of oxidative reactions, with partial oxidation being predominant and total oxidation being secondary and less efficient.

Nonthermal plasma in nitrogen primarily generates high-energy electrons, which drive the reactions through electron impact ionization and excitation. High-energy electrons can excite N_2 molecules to metastable states (e.g., N_2*), which contribute to bond scission indirectly by transferring energy to polymer bonds.[65] Dissociation reactions, such as $N_2 + e \rightarrow 2N + e$, provide reactive atomic nitrogen, but these species are less involved in oxidative pathways than oxygen-based plasmas. Overall, high-energy electrons are the dominant reactive species in N_2 plasma, facilitating bond cleavage, especially with reactive atomic oxygen (O) in polymers through direct electron interactions rather than oxidative mechanisms.

Nonthermal plasma in CO_2 primarily produces CO and ROS (O), with the dissociation reaction $CO_2 + e \rightarrow CO + O + e$, $CO + e \rightarrow C + O + e$. ROS from CO_2 plasma have lower oxidative potential than those derived from O_2 plasma due to the differences in dissociation energy and reactive pathways.[66,67] Atomic oxygen from CO_2 dissociation is less reactive toward initiating chain scission or oxidation compared to the ROS generated in air plasma. In all, CO_2 plasma is less effective for partial oxidation and predominantly generates CO and less-

https://doi.org/10.1021/acs.jpcc.4c07876
J. Phys. Chem. C 2025, 129, 4950−4963

ROS, limiting its impact on oxidative depolymerization compared to air plasma.

The high energy electrons from the C, N, and O atoms play a key role in the plasma to scissor the chemical bonds (3−5 eV in PVA) compared with radicals and excited species.[68−70] Based on the experimental results, N_2 plasma dissipated the most OH groups from the PVA chain. The $OH^•$ radicals have the strongest oxidation ability among the C, N, O, and CO radicals via H abstraction from organic groups and oxidize the alcohol group to ketone group and further acid group, probably some due to the reactive O atoms cracking from $OH^•$.[69−71]

Overall, the PVA depolymerization mechanism is shown in Figure 11. After the high-energy electrons and radicals synergically attack the PVA, the backbone dissociates into smaller fragments, some with the alcohol groups oxidatively dehydrogenating to ketone groups and then cleaving into gas-phase radicals or continuing to oxidize to carboxylic acid groups, while the rest was unoxidized into short-chain solid fragments. Then, the unstable intermediate gas products will diffuse along the catalyst surface and be adsorbed to the surface, increasing the chance of chemical reactions. The subsequent desorption gas species will combine with O* (part of O radicals from TiO_2) and H* via the oxidation or hydrogenation reaction to form small gas molecules like CO_2 and aldehydes as detected by the in situ FTIR, and all three gas plasmas give off the same gaseous products from the previous study.[10] Part of the fragmented solid products will continue to be scissored and hydrogenated to the CH_2 group in the backbone afterward. The subsequent oxidation reaction of the alcohol group in the rest of PVA leads to a carboxylic acid or ketone group. Carboxylic acid will react with PVA to produce PVAc via an esterification reaction. The gas products acetaldehyde and propionaldehyde will further react with the alcohol group in the acid environment to produce cyclic cross-linking structures like PVA−PVAc-PVA-acetal ($O-CH_3CH_2-O$) or PVA−PVAc-PVA-propional ($O-CH_3CH_2CH_2-O$). Given all of the products we found in the gas and solid phases, the catalyst TiO_2 not only facilitates the decomposition of the backbone but also promotes the reaction for alcohol group reduction, gas production, especially CO_2, and the PVAc formation in the solid products. This proposal unveils the complex chemical reactions in plasma chemistry, including dehydrative oxidation, alkylation, esterification, and acetal reactions, and are well validated by the experimental results in our plasma-assisted PVA depolymerization case.

4. CONCLUSIONS

In summary, PVA was effectively depolymerized using a nonthermal air, CO_2, and N_2 plasma generated in a DBD setup with TiO_2 serving as a catalyst. Raman, FTIR, and XAS characterizations confirmed the scission of the C−C backbone and the conversion of the alcohol group to the ketone group in the fragmented polymers. The NMR and MS studies suggested PVAc and the cross-linked structure PVA-aldehyde. TiO_2 as a catalyst with O radicals significantly enhanced the degradation process as evidenced by the evenly distributed plasma reaction on the PVA surface in SEM comparison between the PVA and PVA−TiO_2 mixture. Further XRD and TEM measurements on TiO_2 show no major surface and crystal structure changes, indicating its stability and effectiveness as a catalyst for nonthermal plasma-assisted reactions. This study also found that nitrogen plasma enhances the production of ketone (i.e., carbonyl) groups, while oxygen plasma improves the overall conversion efficiency. These findings align with previous reports on the composition of gas phase products, which showed high selectivity toward carbonyl-containing products, acetaldehyde and propionaldehyde, thereby providing complementary insights into the overall mechanism of nonthermal plasma-assisted polymer depolymerization. This technique serves as a low-energy-cost and efficient method with the rational selection of catalysts and the design of plasma reactions under ambient conditions (25 °C and 1 atm).

■ ASSOCIATED CONTENT

Supporting Information

The Supporting Information is available free of charge at https://pubs.acs.org/doi/10.1021/acs.jpcc.4c07876.

Nonthermal plasma DBD reactor scheme, thermal cracking and other nonthermal plasma methods, SEM and TEM images of catalyst TiO_2 powders, and SEM images of contaminated PVA and PVA−TiO_2 mixture samples (PDF)

■ AUTHOR INFORMATION

Corresponding Authors

Steven S. C. Chuang − *Department of Chemical and Biomolecular Engineering, The University of Akron, Akron, Ohio 44325, United States;* orcid.org/0009-0001-0206-2171; Email: chuang@uakron.edu

Jinghua Guo − *Advanced Light Source, Lawrence Berkeley National Laboratory, Berkeley, California 94720, United States;* orcid.org/0000-0002-8576-2172; Email: jguo@lbl.gov

Jin Zhong Zhang − *Department of Chemistry and Biochemistry, University of California, Santa Cruz, California 95064, United States;* orcid.org/0000-0003-3437-912X; Phone: +1-831-459-3776; Email: zhang@ucsc.edu

Authors

Heng Zhang − *Department of Chemistry and Biochemistry, University of California, Santa Cruz, California 95064, United States;* orcid.org/0000-0001-8521-5403

Aderinsola Oduntan − *Department of Chemical and Biomolecular Engineering, The University of Akron, Akron, Ohio 44325, United States*

Zengqing Zhuo − *Advanced Light Source, Lawrence Berkeley National Laboratory, Berkeley, California 94720, United States;* orcid.org/0000-0001-6602-760X

Complete contact information is available at: https://pubs.acs.org/10.1021/acs.jpcc.4c07876

Notes

The authors declare no competing financial interest.

■ ACKNOWLEDGMENTS

We acknowledge financial support from the National Science Foundation (#2132178). We thank the samples from the Steven lab in the University of Akron. We thank ALS (Advanced Light Source) in the Berkeley National Lab for the support of the XAS experiment, which is in a DOE Office of Science User Facility under contract no. DE-AC02-05CH11231. We thank Lori Etow for the support of the solid-state FTIR measurement. We thank Dr. Tom Yuzvinsky

for assistance with electron microscopy and the W.M. Keck Center for Nanoscale Optofluidics for the use of the FEI Quanta 3D Dualbeam microscope. We also thank Dr. Chengyu Song for the TEM images help and support from the NCEM (National Center for Electron Microscopy) in Berkeley National Lab. Work at the Molecular Foundry was supported by the Office of Science, Office of Basic Energy Sciences, Office of the U.S. Department of Energy under contract no. DE-AC02-05CH11231. We thank Jack Lee and Laura Sanchez at UC Santa Cruz for the NMR and mass spectroscopy measurements. Many thanks to Prof. Rebecca Braslau and Dr. Elizabeth (Betsy) McCord for the helpful discussion.

REFERENCES

(1) Pathak, V. M.; Navneet. Review on the current status of polymer degradation: a microbial approach. *Bioresour. Bioprocess.* **2017**, *4* (1), 15.
(2) Beaumont, C.; Turgeon, J.; Idir, M.; Neusser, D.; Lapointe, R.; Caron, S.; Dupont, W.; D'Astous, D.; Shamsuddin, S.; Hamza, S.; et al. Water-Processable Self-Doped Conducting Polymers via Direct (Hetero)Arylation Polymerization. *Macromolecules* **2021**, *54* (12), 5464−5472.
(3) Schneiderman, D. K.; Hillmyer, M. A. 50th Anniversary Perspective: There Is a Great Future in Sustainable Polymers. *Macromolecules* **2017**, *50* (10), 3733−3749.
(4) Khah, H. M.; Soleimani, O. Properties and Applications of Polymers: A Mini Review. *J. Chem. Rev.* **2023**, *5* (2), 204−220.
(5) Mayadunne, R. T. A.; Jeffery, J.; Moad, G.; Rizzardo, E. Living Free Radical Polymerization with Reversible Addition−Fragmentation Chain Transfer (RAFT Polymerization): Approaches to Star Polymers. *Macromolecules* **2003**, *36* (5), 1505−1513.
(6) Song, J. H.; Murphy, R. J.; Narayan, R.; Davies, G. B. H. Biodegradable and Compostable Alternatives to Conventional Plastics. *Philos. Trans. R. Soc., B* **2009**, *364* (1526), 2127−2139.
(7) Uttiya Dey, U. D. An Approach to Polymer Degradation through Microbes. *IOSR J. Pharm.* **2012**, *2* (3), 385−388.
(8) Uekert, T.; Singh, A.; DesVeaux, J. S.; Ghosh, T.; Bhatt, A.; Yadav, G.; Afzal, S.; Walzberg, J.; Knauer, K. M.; Nicholson, S. R.; et al. Technical, Economic, and Environmental Comparison of Closed-Loop Recycling Technologies for Common Plastics. *ACS Sustain. Chem. Eng.* **2023**, *11* (3), 965−978.
(9) Javed, S.; Vogt, D. Development of Eco-Friendly and Sustainable PET Glycolysis Using Sodium Alkoxides as Catalysts. *ACS Sustain. Chem. Eng.* **2023**, *11* (31), 11541−11547.
(10) Oduntan, A.; Wei, J. F.; Ma, J.; Toskin, A.; Miyoshi, T.; Liu, T.; Chuang, S. S. C. Remarkable Selectivity of Polyvinyl Alcohol Oxidation: An Insight from Ambient Air Plasma in the Presence and Absence of TiO_2. *Appl. Catal. O: Open* **2024**, *192*, 206921.
(11) Bhatnagar, S.; Kumari, R. Bioremediation: A Sustainable Tool for Environmental Management-a Review. *Annu. Rev. Res. Biol.* **2013**, *3* (4), 974−993.
(12) Arutchelvi, J.; Sudhakar, M.; Arkatkar, A. S.; Doble, M.; Bhaduri, S.; Uppara, P. V. Biodegradation of Polyethylene and Polypropylene. *Indian J. Biotechnol.* **2008**, *7*, 9−22.
(13) Lee, Y.; Cho, J.; Sohn, J.; Kim, C. Health Effects of Microplastic Exposures: Current Issues and Perspectives in South Korea. *Yonsei Med. J.* **2023**, *64* (5), 301−308.
(14) Ayer, M. A.; Simon, Y. C.; Weder, C. Azo-Containing Polymers with Degradation On-Demand Feature. *Macromolecules* **2016**, *49* (8), 2917−2927.
(15) Steinman, N. Y.; Starr, R. L.; Brucks, S. D.; Belay, C.; Meir, R.; Golenser, J.; Campos, L. M.; Domb, A. J. Cyclopropenium-Based Biodegradable Polymers. *Macromolecules* **2019**, *52* (9), 3543−3550.
(16) Chuang, S. S. C.; Huhe, F.; Oduntan, A.; Peng, Z. Transient Responses of Product Formation in Nonthermal Plasma-Assisted D_2O-CO_2-Rubber Reaction. *Catal. Commun.* **2023**, *180*, 106707.
(17) Nguyen, H. M.; Carreon, M. L. Non-Thermal Plasma-Assisted Deconstruction of High-Density Polyethylene to Hydrogen and Light Hydrocarbons over Hollow ZSM-5 Microspheres. *ACS Sustain. Chem. Eng.* **2022**, *10* (29), 9480−9491.
(18) Yao, L.; King, J.; Wu, D.; Chuang, S. S. C.; Peng, Z. Non-Thermal Plasma-Assisted Hydrogenolysis of Polyethylene to Light Hydrocarbons. *Catal. Commun.* **2021**, *150*, 106274.
(19) Aminu, I.; Nahil, M. A.; Williams, P. T. Hydrogen Production by Pyrolysis−Nonthermal Plasma/Catalytic Reforming of Waste Plastic over Different Catalyst Support Materials. *Energy Fuels* **2022**, *36* (7), 3788−3801.
(20) Pishva, P.; Li, J.; Xie, R.; Tang, J.; Nandy, P.; Farouk, T.; Guo, J.; Peng, Z. Nonthermal Hydrogen Plasma-Enabled Ambient, Fast Lignin Hydrogenolysis to Valuable Chemicals and Bio-Oils. *Chem. Eng. J.* **2024**, *501*, 157776.
(21) Miskolczi, N.; Angyal, A.; Bartha, L.; Valkai, I. Fuels by Pyrolysis of Waste Plastics from Agricultural and Packaging Sectors in a Pilot Scale Reactor. *Fuel Process. Technol.* **2009**, *90* (7), 1032−1040.
(22) Lee, K.-H. Effects of the Types of Zeolites on Catalytic Upgrading of Pyrolysis Wax Oil. *J. Anal. Appl. Pyrolysis* **2012**, *94*, 209−214.
(23) Xu, C.; Luo, J.-L. Understanding the Light-Induced Oxygen Vacancy in the Photochemical Conversion. *J. Phys.: Energy* **2023**, *5* (1), 011001.
(24) Bogaerts, A.; Tu, X.; Whitehead, J. C.; Centi, G.; Lefferts, L.; Guaitella, O.; Azzolina-Jury, F.; Kim, H.-H.; Murphy, A. B.; Schneider, W. F.; Nozaki, T.; Hicks, J. C.; Rousseau, A.; Thevenet, F.; Khacef, A.; Carreon, M. The 2020 Plasma Catalysis Roadmap. *J. Phys. D: Appl. Phys.* **2020**, *53* (44), 443001.
(25) Khatibi, M.; Nahil, M. A.; Williams, P. T. Interaction of Furfural and Hexadecane as Bio-Oil and Plastics Pyro-Oil Model Compounds with Non-Thermal Plasma Processing as a Route to *in-Situ* Hydrogen Donor Upgrading of Bio-Oil. *Biomass Bioenergy* **2024**, *187*, 107301.
(26) Ren, L.; Mao, M.; Li, Y.; Lan, L.; Zhang, Z.; Zhao, X. Novel Photothermocatalytic Synergetic Effect Leads to High Catalytic Activity and Excellent Durability of Anatase TiO_2 Nanosheets with Dominant {001} Facets for Benzene Abatement. *Appl. Catal., B* **2016**, *198*, 303−310.
(27) Bhat, N. V.; Nate, M. M.; Kurup, M. B.; Bambole, V. A.; Sabharwal, S. Effect of γ-Radiation on the Structure and Morphology of Polyvinyl Alcohol Films. *Nucl. Instrum. Methods Phys. Res., Sect. B* **2005**, *237* (3), 585−592.
(28) Al-Taweel, S. S.; Saud, H. R. New Route for Synthesis of Pure Anatase TiO_2 Nanoparticles via Utrasound-Assisted Sol-Gel Method. *J. Chem. Pharm. Res.* **2016**, *8* (2), 620−626.
(29) Taudul, B.; Tielens, F.; Calatayud, M. On the Origin of Raman Activity in Anatase TiO_2 (Nano)Materials: An Ab Initio Investigation of Surface and Size Effects. *Nanomaterials* **2023**, *13* (12), 1856.
(30) Appadurai, T.; Subramaniyam, C. M.; Kuppusamy, R.; Karazhanov, S.; Subramanian, B. Electrochemical Performance of Nitrogen-Doped TiO_2 Nanotubes as Electrode Material for Supercapacitor and Li-Ion Battery. *Molecules* **2019**, *24*, 2952.
(31) Challagulla, S.; Tarafder, K.; Ganesan, R.; Roy, S. Structure Sensitive Photocatalytic Reduction of Nitroarenes over TiO_2. *Sci. Rep.* **2017**, *7* (1), 8783.
(32) Kamegawa, T.; Irikawa, K.; Yamashita, H. Multifunctional Surface Designed by Nanocomposite Coating of Polytetrafluoroethylene and TiO_2 Photocatalyst: Self-Cleaning and Superhydrophobicity. *Sci. Rep.* **2017**, *7* (1), 13628.
(33) Bakar, S. A.; Ribeiro, C. Nitrogen-Doped Titanium Dioxide: An Overview of Material Design and Dimensionality Effect over Modern Applications. *J. Photochem. Photobiol., C* **2016**, *27*, 1−29.
(34) Balog, A.-; Samu, G. F.; Pető, S.; Janáky, C. The Mystery of Black TiO_2: Insights from Combined Surface Science and In Situ Electrochemical Methods. *ACS Mater. Au* **2021**, *1* (2), 157−168.
(35) Deng, H.; Yuan, L.; Li, Z.; Wang, D.; Wang, X.; Liang, P.; Wang, L.; Liu, Y.; Fu, Y.; Chang, Z.; et al. A Hybrid Amorphous/Crystalline TiO_2 Material with Enhanced Photocatalytic Performance. *Adv. Sustain. Syst.* **2022**, *6* (12), 2200316.

https://doi.org/10.1021/acs.jpcc.4c07876
J. Phys. Chem. C 2025, 129, 4950−4963

(36) Scally, L.; Gulan, M.; Weigang, L.; Cullen, P. J.; Milosavljevic, V. Significance of a Non-Thermal Plasma Treatment on LDPE Biodegradation with Pseudomonas Aeruginosa. *Materials* **2018**, *11* (10), 1925.
(37) Remiš, T.; Bělský, P.; Kovářík, T.; Kadlec, J.; Ghafouri Azar, M.; Medlín, R.; Vavruňková, V.; Deshmukh, K.; Sadasivuni, K. K. Study on Structure, Thermal Behavior, and Viscoelastic Properties of Nanodiamond-Reinforced Poly (Vinyl Alcohol) Nanocomposites. *Polymers* **2021**, *13* (9), 1426.
(38) Weon, S.; Choi, W. TiO_2 Nanotubes with Open Channels as Deactivation-Resistant Photocatalyst for the Degradation of Volatile Organic Compounds. *Environ. Sci. Technol.* **2016**, *50* (5), 2556−2563.
(39) Sofyan, N.; Ridhova, A.; Yuwono, A. H.; Udhiarto, A. Preparation of Anatase TiO_2 Nanoparticles Using Low Hydrothermal Temperature for Dye-Sensitized Solar Cell. *IOP Conf. Ser. Mater. Sci. Eng.* **2018**, *316*, 012055.
(40) Sridevi, A.; Ramji, B. R.; Prasanna Venkatesan, G. K. D.; Sugumaran, V.; Selvakumar, P. A Facile Synthesis of TiO_2/BiOCl and TiO_2/BiOCl/La_2O_3 Heterostructure Photocatalyst for Enhanced Charge Separation Efficiency with Improved UV-Light Catalytic Activity towards Rhodamine B and Reactive Yellow 86. *Inorg. Chem. Commun.* **2021**, *130*, 108715.
(41) Zare, M. H.; Mehrabani-Zeinabad, A. Photocatalytic Activity of ZrO_2/TiO_2/Fe_3O_4 Ternary Nanocomposite for the Degradation of Naproxen: Characterization and Optimization Using Response Surface Methodology. *Sci. Rep.* **2022**, *12* (1), 10388.
(42) Uddin, M. J.; Cesano, F.; Chowdhury, A. R.; Trad, T.; Cravanzola, S.; Martra, G.; Mino, L.; Zecchina, A.; Scarano, D. Surface Structure and Phase Composition of TiO_2 P25 Particles After Thermal Treatments and HF Etching. *Front. Mater.* **2020**, *7*, 531722.
(43) Marka, S. K.; Sindam, B.; James Raju, K. C.; Srikanth, V. V. S. S. Flexible Few-Layered Graphene/Poly Vinyl Alcohol Composite Sheets: Synthesis, Characterization and EMI Shielding in X-Band through the Absorption Mechanism. *RSC Adv.* **2015**, *5* (46), 36498−36506.
(44) Kharazmi, A.; Faraji, N.; Mat Hussin, R.; Saion, E.; Yunus, W. M. M.; Behzad, K. Structural, Optical, Opto-Thermal and Thermal Properties of ZnS−PVA Nanofluids Synthesized through a Radiolytic Approach. *Beilstein J. Nanotechnol.* **2015**, *6* (1), 529−536.
(45) Korbag, I.; Mohamed Saleh, S. Studies on the Formation of Intermolecular Interactions and Structural Characterization of Polyvinyl Alcohol/Lignin Film. *Int. J. Environ.* **2016**, *73* (2), 226−235.
(46) Jipa, I.; Stoica, A.; Stroescu, M.; Dobre, L.-M.; Dobre, T.; Jinga, S.; Tardei, C. Potassium Sorbate Release from Poly(Vinyl Alcohol)−Bacterial Cellulose Films. *Chem. Pap.* **2012**, *66* (2), 138−143.
(47) Zárate, I. A.; Aguilar-Bolados, H.; Yazdani-Pedram, M.; Pizarro, G. d. C.; Neira-Carrillo, A. In Vitro Hyperthermia Evaluation of Electrospun Polymer Composite Fibers Loaded with Reduced Graphene Oxide. *Polymers* **2020**, *12* (11), 2663.
(48) P D'Amelia, R.; Kimura, M. W.; Mancuso, J. Synthesis and Characterization of Polyvinyl Alkyl Ester and Polyvinyl Alcohol Homopolymers and Blends of Polyvinyl Alkyl Esters. *J. Polym. Biopolym. Phys. Chem.* **2021**, *9* (1), 1−12.
(49) Cheung, M. K.; Wang, J.; Zheng, S.; Mi, Y. Miscibility of Poly(Epichlorohydrin)/Poly(Vinyl Acetate) Blends Investigated with High-Resolution Solid-State ^{13}C NMR. *Polymer* **2000**, *41* (4), 1469−1474.
(50) Geng, S.; Shah, F. U.; Liu, P.; Antzutkin, O. N.; Oksman, K. Plasticizing and Crosslinking Effects of Borate Additives on the Structure and Properties of Poly(Vinyl Acetate). *RSC Adv.* **2017**, *7* (13), 7483−7491.
(51) Caló, E.; Barros, J. M. S. d.; Fernández-Gutiérrez, M.; San Román, J.; Ballamy, L.; Khutoryanskiy, V. V. Antimicrobial Hydrogels Based on Autoclaved Poly(Vinyl Alcohol) and Poly(Methyl Vinyl Ether- Alt -Maleic Anhydride) Mixtures for Wound Care Applications. *RSC Adv.* **2016**, *6* (60), 55211−55219.
(52) Audette, Y.; Congreves, K. A.; Schneider, K.; Zaro, G. C.; Nunes, A. L. P.; Zhang, H.; Voroney, P. R. The Effect of Agroecosystem Management on the Distribution of C Functional Groups in Soil Organic Matter: A Review. *Biol. Fertil. Soils* **2021**, *57*, 881−894.
(53) Khatibi, M.; Nahil, M. A.; Williams, P. T. Improving the Quality of Bio-Oil Using the Interaction of Plastics and Biomass through Copyrolysis Coupled with Nonthermal Plasma Processing. *Energy Fuels* **2024**, *38* (2), 1240−1257.
(54) Gao, X.; Lin, Z.; Li, T.; Huang, L.; Zhang, J.; Askari, S.; Dewangan, N.; Jangam, A.; Kawi, S. Recent Developments in Dielectric Barrier Discharge Plasma-Assisted Catalytic Dry Reforming of Methane over Ni-Based Catalysts. *Catalysts* **2021**, *11* (4), 455.
(55) Meng, F.; Li, X.; Liang, H.; Wang, G.; Lu, L.; Liu, J. Non-Thermal Plasma Degradation of Tar in Gasification Syngas. *Chem. Eng. Process.: Process Intensif.* **2019**, *145*, 107656.
(56) Hossain, U. H.; Seidl, T.; Ensinger, W. Combined in situ infrared and Mass Spectrometric Analysis of high-energy heavy ion induced degradation of polyvinyl polymers. *Polym. Chem.* **2014**, *5* (3), 1001−1012.
(57) Bian, W.; Song, X.; Liu, D.; Zhang, J.; Chen, X. Actions of Nitrogen Plasma in the 4-Chrolophenol Degradation by Pulsed High-Voltage Discharge with Bubbling Gas. *Chem. Eng. J.* **2013**, *219*, 385−394.
(58) Sharma, V.; Hosoi, K.; Mori, T.; Kuroda, S. Electrical and Optical Characterization of Cold Atmospheric Pressure Plasma Jet and the Effects of N_2 Gas on Argon Plasma Discharge. *Appl. Mech. Mater.* **2012**, *268−270*, 522−528.
(59) Li, M.; Xu, G.; Tian, Y.; Chen, L.; Fu, H. Carbon Dioxide Reforming of Methane Using DC Corona Discharge Plasma Reaction. *J. Phys. Chem. A* **2004**, *108* (10), 1687−1693.
(60) Hagstrum, H. D. Ionization by Electron Impact in CO, N_2, NO, and O_2. *Rev. Mod. Phys.* **1951**, *23* (3), 185−203.
(61) Takamatsu, T.; Uehara, K.; Sasaki, Y.; Miyahara, H.; Matsumura, Y.; Iwasawa, A.; Ito, N.; Azuma, T.; Kohno, M.; Okino, A. Investigation of Reactive Species Using Various Gas Plasmas. *RSC Adv.* **2014**, *4* (75), 39901−39905.
(62) Ahn, H. J.; Kim, K. I.; Hoan, N. N.; Kim, C. H.; Moon, E.; Choi, K. S.; Yang, S. S.; Lee, S. Targeting Cancer Cells with Reactive Oxygen and Nitrogen Species Generated by Atmospheric-Pressure Air Plasma. *PLoS One* **2014**, *9* (1), No. e86173.
(63) Privat-Maldonado, A.; Schmidt, A.; Lin, A.; Weltmann, D.; Wende, K.; Bogaerts, A.; Bekeschus, S. ROS from Physical Plasmas: Redox Chemistry for Biomedical Therapy. *Oxid. Med. Cell. Longevity* **2019**, *2019* (1), 9062098.
(64) Kim, S. J.; Chung, T. H. Cold atmospheric plasma jet-generated RONS and their selective effects on normal and carcinoma cells. *Sci. Rep.* **2016**, *6* (1), 20332.
(65) Laput, O. A.; Vasenina, I. V.; Korzhova, A. G.; Bryuzgina, A. A.; Khomutova, U. V.; Tuyakova, S. G.; Akhmadeev, Y. H.; Shugurov, V. V.; Bolbasov, E. N.; Tverdokhlebov, S. I.; Chernyavskii, A. V.; Kurzina, I. A. Effect of Nitrogen Arc Discharge Plasma Treatment on Physicochemical Properties and Biocompatibility of PLA-Based Scaffolds. *Polymers* **2023**, *15* (16), 3381.
(66) Li, P.; Wang, J.; Xie, J. Excitation of Reactive Oxygen Species and Damage to the Cell Membrane, Protein, and DNA are Important Inhibition Mechanisms of CO_2 on Shewanella putrefaciens at 4 °C. *J. Agric. Food Chem.* **2024**, *72* (31), 17559−17571.
(67) Khatun, R.; Pal, R. S.; Shoeb, M. A.; Khurana, D.; Singhl, S.; Siddiqui, N.; Poddar, M. K.; Khan, T. S.; Bal, R. Generation of active oxygen species by CO_2 dissociation over defect-rich Ni-Pt/CeO_2 catalyst for boosting methane activation in low-temperature dry reforming: Experimental and theoretical study. *Appl. Catal., B* **2024**, *340*, 123243.
(68) Atkins, P.; de Paula, J. *Physical Chemistry*, 10th ed.; Oxford University Press: Oxford, 2014.
(69) Wardman, P. Reduction Potentials of One-Electron Couples Involving Free Radicals in Aqueous Solution. *J. Phys. Chem. Ref. Data* **1989**, *18* (4), 1637−1755.
(70) Buxton, G. V.; Greenstock, C. L.; Helman, W. P.; Ross, A. B. Critical Review of Rate Constants for Reactions of Hydrated

https://doi.org/10.1021/acs.jpcc.4c07876
J. Phys. Chem. C 2025, 129, 4950−4963

Electrons, Hydrogen Atoms and Hydroxyl Radicals in Aqueous Solution. *J. Phys. Chem. Ref. Data* **1988**, *17* (2), 513−886.
(71) Neta, P.; Huie, R. E.; Ross, A. B. Rate Constants for Reactions of Inorganic Radicals in Aqueous Solution. *J. Phys. Chem. Ref. Data* **1988**, *17* (3), 1027−1284.

https://doi.org/10.1021/acs.jpcc.4c07876
J. Phys. Chem. C 2025, 129, 4950−4963